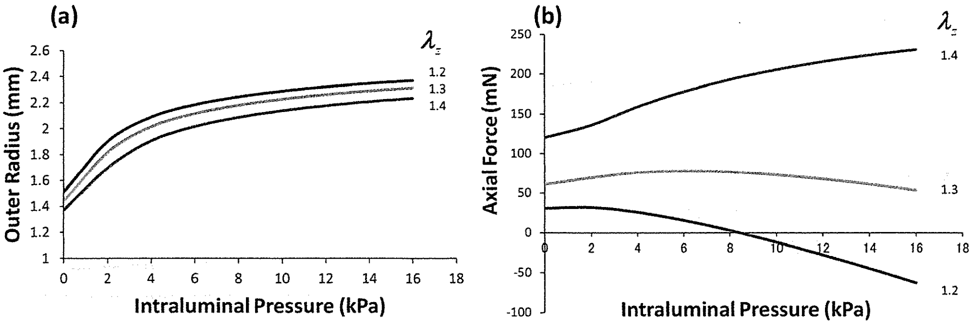

Fig. 3 Curves of outer radius versus intraluminal pressure (*a*) and axial force versus intraluminal pressure (*b*)

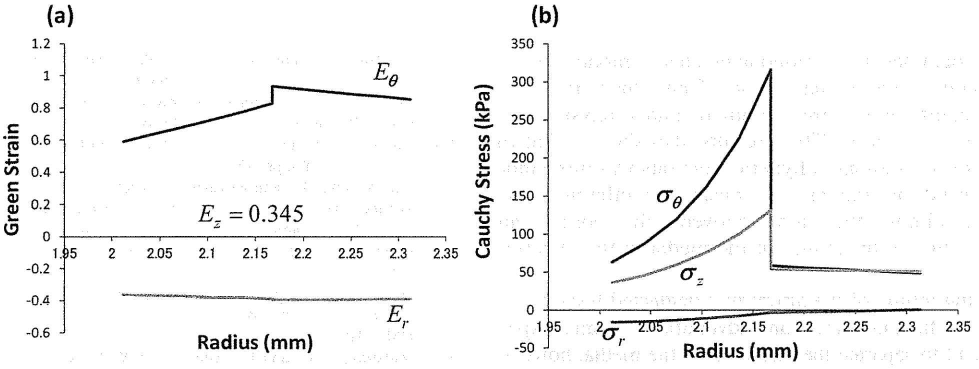

Fig. 4 Distributions of strain (*a*) and stress (*b*) at intraluminal pressure of 16 kPa (120 mmHg). The boundary between media and adventitia is a position where the discontinuity of distributions of strain and stress appears.

intraluminal pressure relations and the axial force versus intraluminal pressure relations as the intraluminal pressures increase from 0 to 16 kPa (120 mmHg) for axial stretch ratios of 1.2, 1.3, and 1.4. These results are similar to the data for the porcine LAD by Wang et al. [25] and validate the model used in this study. It should be noted that the axial stretch ratios in Fig. 3 are defined with regard to a stress-free state, although the experimental axial stretch ratio was defined with regard to an unloaded state. However, this difference is very small, as shown in Fig. 2, and is experimentally negligible.

The strain and stress distributions at an intraluminal pressure of 16 kPa and an axial stretch ratio of 1.3 are shown in Fig. 4. This pressure was chosen because it is a physiological one. The axial stretch ratio is also considered as a physiological one from a review by Humphrey et al. [27], who indicated that the axial force is almost constant with a change of intraluminal pressure under in situ axial stretch. Of the three axial stretch ratios, an axial stretch of 1.3 almost satisfies this condition. The boundary between media and adventitia is located at the radius where the discontinuity of distribution occurs in Fig. 4. The circumferential strain in the media linearly increases from the intraluminal surface to the boundary (Eqs. (8) and (10)). This is because of the opening angle of the medial layer sector being larger than π(rad) as explained above. On the other hand, the opening angle of the adventitial layer is smaller than π(rad). The circumferential strain linearly decreases from the boundary to the outer surface. The circumferential stress distribution drastically changes between the media and the adventitia. The circumferential stress at the boundary is almost six times larger than the stress at the intraluminal surface in the media. On the other hand, the stress is low and almost uniform in the adventitia. It is because of the difference of the constants in the strain energy function. At axial stretch ratios of 1.3 and 1.4, the media is much stiffer than the adventitia in the circumferential direction, as shown by Wang et al. [19]. This explains the drastic stress difference between the media and adventitia, although the value of circumferential strain is not too different between the two layers. The radial strain is almost uniform through the wall thickness.

Figure 5 shows the strain and stress distributions at an intraluminal pressure 24 kPa (180 mmHg). This pressure is higher than the maximal experimental value [19]. However, an extrapolation may be allowed. The object of this calculation is to understand the change in stress distribution during hypertension. The pattern of the strain distribution at a pressure of 24 kPa is similar to that at a pressure of 16 kPa because the radius change is small under higher pressures, although the value of circumferential stress increases almost twice at a pressure of 24 kPa. In *in vivo* hypertension, a remodeling of vessel wall occurs as demonstrated by Matsumoto and Hayashi [14]. This study suggests that hypertension may cause a remodeling in the media rather than in the adventitia.

4 Discussion

The magnitude of the residual stress of an artery is extremely small compared with the stress under physiological conditions. Thus it is not sufficient to relieve all residual stress by making a radial cut of a sliced ring of the artery. In fact, Matsumoto and Sato [28] showed a change in opening angles among four separated layers in a bovine thoracic aorta. They found that the opening angle linearly decreases from the inner to the outer layer. For coronary arteries, the media and adventitia were separated and each layer was sectioned radially. While these treatments may not be sufficient to relieve all residual stress, it is impossible to separate many layers and then obtain the three-dimensional nonlinear constitutive law for each layer.

Matsumoto and Hayashi [14] showed that the circumferential stress gradient through the wall of a normal rat aorta was larger than that expected from homeostatic control with remodeling,

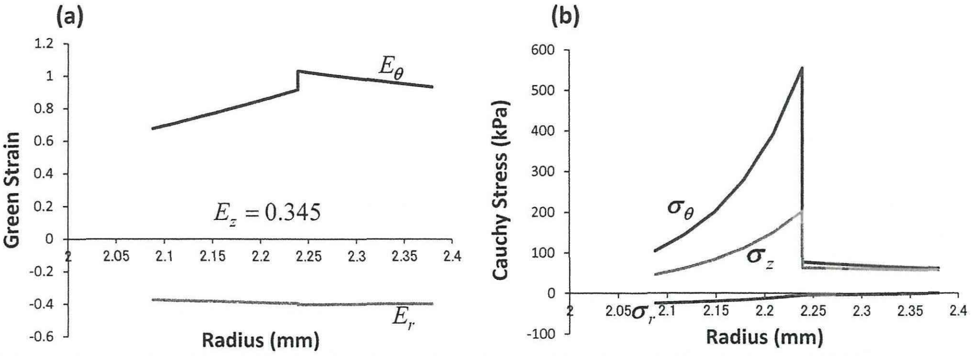

Fig. 5 Distributions of strain (*a*) and stress (*b*) at intraluminal pressure of 24 kPa (180 mmHg). The boundary between media and adventitia is a position where the discontinuity of distributions of strain and stress appears.

although it was obtained by a monolayer elastic model and the opening angle being smaller than π(rad). Thus, there may be a considerable circumferential stress gradient under physiological conditions of normal arteries. Their results also showed that the circumferential stress gradient in hypertensive rats was more moderate than that in normal rats and the mean circumferential systolic stress was almost the same between the normal and hypertensive rats due to thickening of the media in the hypertensive rats.

In this study, the intima of the artery was neglected because it is significantly thinner than the media and adventitia. In animal experiments, it is difficult to separate the intima from the media, however, Holzapfel et al. [16] studied human coronary arteries. They showed that the intima of aged human arteries thickens and can be separated and determined the parameters of a strain energy function by the stretch experiments for strip specimens of each layer.

It is well known that shear stress induced by blood flow is deeply related to localization of atherosclerotic lesions [29], although the role of stress in an arterial wall is not known better than that for shear stress. We also need to know the pathological role of the wall stress. To attain this objective, we need to know the accurate stress distribution in the vessel walls.

5 Conclusion

Strain and stress distribution in the porcine LAD wall was analyzed on the basis of a bilayer elastic model consisting of the media and adventitia considering residual stress (strain). This study showed that peak circumferential stress appears at the boundary in the media region under physiological conditions. The high stress in the media compared with the stress in the adventitia may induce a remodeling of the media during hypertension.

References

[1] Fung, Y. C., 1983, "What Principle Governs the Stress Distribution in Living Organs?" *Biomechanics in China, Japan, and U.S.A.*, Y. C. Fung, E. Fukada, and W. Junjian, eds., Science Press, Beijing, pp. 1–13.
[2] Fung, Y. C., 1984, *Biodynamics: Circulation*, Springer-Verlag, New York.
[3] Liu, S. Q., and Fung, Y. C., 1988, "Zero-Stress States of Arteries," J. Biomech. Eng., **110**, pp. 82–84.
[4] Omens, J. H., and Fung, Y. C., 1990, "Residual Strain in Rat Left Ventricle," Circ. Res., **66**, pp. 37–45.
[5] Vaishnav, R. N., and Vossoughi, J., 1983, "Estimation of Residual Strains in Aortic Segments," *Biomedical Engineering II: Recent Developments*, C. W. Hall, ed., Pergamon Press, New York, pp. 330–333.
[6] Vaishnav, R. N., and Vossoughi, J., 1987, "Residual Stress and Strain in Aortic Segments," J. Biomech., **20**, pp. 235–239.
[7] Takamizawa, K., and Hayashi, K., 1987, "Strain Energy Density Function and Uniform Strain Hypothesis for Arterial Mechanics," J. Biomech., **20**, pp. 7–17.
[8] Chuong, C. J., and Fung, Y. C., 1983, "Three-Dimensional Stress Distribution in Arteries," J. Biomech. Eng., **105**, pp. 268–274.
[9] Mirsky, I., 1973, "Ventricular and Arterial Wall Stresses Based on Large Deformation Theories," Biophys. J., **13**, pp. 1141–1159.
[10] Chuong, C. J., and Fung Y. C., 1986, "On Residual Stress in Arteries," J. Biomech. Eng., **108**, pp. 189–192.
[11] Takamizawa, K., and Hayashi, K., 1988, "Uniform Strain Hypothesis and Thin-Walled Theory in Arterial Mechanics," Biorheology, **25**, pp. 555–565.
[12] Fung, Y. C., and Liu, S. Q., 1991, "Change of Zero-Stress State of Rat Pulmonary Arteries in Hypoxic Hypertension," J. Appl. Physiol., **70**, pp. 2455–2470.
[13] Guo, X., Lu, X., and Kassab, G. S., 2005, "Transmural Strain Distribution in the Blood Vessel Wall," Am. J. Physiol. Heart Circ. Physiol., **288**, pp. H881–H886.
[14] Matsumoto, T., and Hayashi, K., 1996, "Stress and Strain Distribution in Hypertensive and Normotensive Rat Aorta Considering Residual Strain," J. Biomech. Eng., **118**, pp. 62–73.
[15] Rhodin, J. A. G., 1980, "Architecture of the Vessel Wall," *Handbook of Physiology*, Sec. 2, Vol. II, D. F. Bohr, A. D. Somlyo, and H. V. Sparks, eds., American Physiological Society, Bethesda, MD, pp. 1–31.
[16] Holzapfel, G. A., Sommer, G., Gasser, C. T., and Regitnig, P., 2005, "Determination of Layer-Specific Mechanical Properties of Human Coronary Arteries With Nonatherosclerotic Intimal Thickening and Related Constitutive Modeling," Am. J. Physiol. Heart Circ. Physiol., **289**, pp. H2048–H2058.
[17] von Maltzhan, W. W., Warriyar, R. G., and Keitzer, W. F., 1984, "Experimental Measurements of Elastic Properties of Media and Adventitia of Bovine Carotid Arteries," J. Biomech., **17**, pp. 839–847.
[18] Fung, Y. C., Fronec, K., and Patitucci, P., 1979, "Pseudoelasticity of Arteries and the Choice of its Mathematical Expression," Am. J. Physiol. Heart Circ. Physiol., **237**, pp. H620–H631.
[19] Wang, C., Garcia, M., Lu, X., Laniar, Y., and Kassab, G. S., 2006, "Three-Dimensional Mechanical Properties of Porcine Coronary Arteries: A Validated Two-Layer Model," Am. J. Physiol. Heart Circ. Physiol., **291**, pp. H1200–H1209.
[20] Takamizawa, K., 2009, "Three-Dimensional Stress and Strain Distribution in a Two-Layer Model of a Coronary Artery," J. Biorheology, **23**, pp. 49–55.
[21] Klarbring, A., Olsson, T., and Stålhand, J., 2007, "Theory of Residual Stress With Application to an Arterial Geometry," Arch. Mech., **59**, pp. 341–364.
[22] Takamizawa, K., and Matsuda, T., 1990, "Kinematics for Bodies Undergoing Residual Stress and Its Applications to the Left Ventricle," J. Appl. Mech., **57**, pp. 321–329.
[23] Patel, D. J., and Fry, D. L., 1969, "The Elastic Symmetry of Arterial Segments in Dogs," Circ. Res., **24**, pp. 1–8.
[24] Lu, X., Pandit, A., and Kassab, G. S., 2004, "Biaxial Incremental Homeostatic Elastic Moduli of Coronary Artery: Two-Layer Model," Am. J. Physiol. Heart Circ. Physiol., **287**, pp. H1663–H1669.
[25] Wang, C., Zhang, W., and Kassab, G. S., 2008, "The Validation of a Generalized Hooke's Law for Coronary Arteries," Am. J. Physiol. Heart Circ. Physiol., **294**, pp. H66–H73.
[26] Fung, Y. C., 1965, *Foundations of Solid Mechanics*, Prentice-Hall, NJ.
[27] Humphrey, J. D., Eberth, J. F., Dye, W. W., and Gleason, R. L., 2009, "Fundamental Role of Axial Stress in Compensatory Adaptations by Arteries," J. Biomech., **42**, pp. 1–8.
[28] Matsumoto, T., and Sato, M., 2002, "Analysis of Stress and Strain Distribution in the Artery Wall Consisted of Layers with Different Elastic Modulus and Opening Angle," JSME Int. J. Ser. C, **45**, pp. 906–912.
[29] Patel, D. J., and Vaishnav, R. N., 1980, *Basic Hemodynamics and Its Role in Disease Processes*, University Park Press, Baltimore, MD.

Non-Euclidean Stress-Free Configuration of Arteries Accounting for Curl of Axial Strips Sectioned From Vessels

Keiichi Takamizawa[1]
e-mail: ktaka@ncvc.go.jp

Yasuhide Nakayama

Department of Biomedical Engineering,
National Cerebral and Cardiovascular Center
Research Institute, 5-7-1 Fujishirodai,
Suita, Osaka 565-8565, Japan

It is well known that arteries are subject to residual stress. In earlier studies, the residual stress in the arterial ring relieved by a radial cut was considered in stress analysis. However, it has been found that axial strips sectioned from arteries also curled into arcs, showing that the axial residual stresses were relieved from the arterial walls. The combined relief of circumferential and axial residual stresses must be considered to accurately analyze stress and strain distributions under physiological loading conditions. In the present study, a mathematical model of a stress-free configuration of artery was proposed using Riemannian geometry. Stress analysis for arterial walls under unloaded and physiologically loaded conditions was performed using exponential strain energy functions for porcine and human common carotid arteries. In the porcine artery, the circumferential stress distribution under physiological loading became uniform compared with that without axial residual strain, whereas a gradient of axial stress distribution increased through the wall thickness. This behavior showed almost the same pattern that was observed in a recent study in which approximate analysis accounting for circumferential and axial residual strains was performed, whereas the circumferential and axial stresses increased from the inner surface to the outer surface under a physiological condition in the human common carotid artery of a two-layer model based on data of other recent studies. In both analyses, Riemannian geometry was appropriate to define the stress-free configurations of the arterial walls with both circumferential and axial residual strains. [DOI: 10.1115/1.4025328]

Keywords: residual stress, arteries, stress-free configuration, Riemannian geometry

1 Introduction

Residual stress plays an important role in the stress distribution of cardiovascular tissues [1]. The importance of residual stress in an artery was demonstrated by Chuong and Fung [2], who analyzed stress under physiological loadings. Thereafter, the radially cut open arterial ring was implemented in stress analysis for the arterial wall. It is important that axial residual strain exists and that it may significantly vary throughout the arterial wall [3,4]. Circumferential and axial residual strains were studied in detail by Holzapfel et al. [5] in human aortas. Holzapfel and Ogden [6] analyzed the residual stretch ratios and stresses on the basis of the data from the above investigation [5] using the neo-Hookean strain energy function for a three layer model. Using the Fung-type strain energy function [7,8], Wang and Gleason [9] analyzed stress distribution in an artery wall under a physiological loaded condition accounting for circumferential and longitudinal residual strains and showed that the circumferential stress distribution through the wall thickness became uniform compared with the case of no longitudinal residual strain whereas the gradient of longitudinal stress increased. Wang and Gleason [9] considered both the circumferential and longitudinal residual strains, although their mathematical analysis was an approximation. A mathematical model to analyze the stress in arterial walls accounting for both circumferential and axial residual strains has not been proposed yet.

In the present paper, we assumed that both the opened-up ring cut radially and curled axial strip are stress free and showed that Riemannian geometry is appropriate to define a stress-free configuration [10,11] of an arterial wall (i.e., in general, a stress-free configuration of an artery may be a three-dimensional non-Euclidean manifold). We analyzed stress in a porcine common carotid artery based on one-layer model [9] using a stress-free configuration and the Fung-type strain energy function to validate the method presented in this paper and a human common carotid artery based on two-layer model using stress-free configurations [12] and a strain energy function [13,14] with constants determined by Sommer and Holzapfel [14].

2 Methods

2.1 Kinematics. As discussed previously [10,11], a stress-free configuration for a body with residual stress may be generally defined as a Riemannian manifold. In this study, we briefly describe this theory. Let $\mathscr{B}$ be a set of material points of a considered solid body and $\langle O; x^k; g_{kl}\rangle$ a curvilinear coordinate system in a three-dimensional Euclidean space $\mathbf{E}^3$. Here, O is the origin of the coordinate system, x^k $(k=1, 2, 3)$ coordinates, and g_{kl} components of a metric tensor of the coordinate system. Because we treated a thick-walled cylindrical vessel, a cylindrical coordinate system $x^1=\theta$, $x^2=z$, and $x^3=r$ with components of a metric tensor $g_{11}=g_{\theta\theta}=r^2$, $g_{22}=g_{zz}=1$, $g_{33}=g_{rr}=1$, and $g_{kl}=0 (k\neq l)$ was adopted.

The current configuration $\chi:\mathscr{B}\rightarrow\mathbf{E}^3$ is a configuration that maps a material point p to $x=(x^1, x^2, x^3)=\chi(p)$. The configuration χ is denoted by κ for a configuration of the unloaded state. In this case, the material point p is mapped as $\xi=(\xi^1, \xi^2, \xi^3)=\kappa(p)$ with components of a metric tensor $\gamma_{\alpha\beta}=g_{\alpha\beta}(\xi)$. For the unloaded configuration, a cylindrical coordinate system $\xi^1=\vartheta$, $\xi^2=\zeta$, and $\xi^3=\rho$ with $\gamma_{11}=\gamma_{\vartheta\vartheta}=\rho^2$, $\gamma_{22}=\gamma_{\zeta\zeta}=1$, $\gamma_{33}=\gamma_{\rho\rho}=1$, and $\gamma_{\alpha\beta}=0(\alpha\neq\beta)$ was adopted. If there is no residual stress, κ is considered a stress-free reference configuration. In later paragraphs, we treated unloaded separate segments for an adventitia and a media-intima of an artery, whereas in the next two paragraphs we expressed a stress-free configuration for a one layer model to avoid complexity of symbols.

Even if a solid body $\kappa(\mathscr{B})$ has residual stress, we may introduce components of a metric tensor $\eta_{\alpha\beta}$ to obtain a stress-free configuration. We shall call the solid body $\kappa(\mathscr{B})$ with components of the metric tensor $\eta_{\alpha\beta}$ Riemannian stress-free configuration. The infinitesimal small distance ds between two material points in the stress-free body is given by the following equation:

$$ds^2=\eta_{\alpha\beta}d\xi^\alpha d\xi^\beta \tag{1}$$

This infinitesimal quadratic form defines the Riemannian stress-free configuration. The Green strain of a current configuration with regard to the Riemannian stress-free configuration is defined by the following equation:

$$E_{\alpha\beta}=\frac{1}{2}\left(\frac{\partial x^k}{\partial\xi^\alpha}\frac{\partial x^l}{\partial\xi^\beta}g_{kl}-\eta_{\alpha\beta}\right) \tag{2}$$

The covariant components of the Riemann–Christoffel tensor are defined as follows [15]:

---

[1] Corresponding author.

Contributed by the Bioengineering Division of ASME for publication in the Journal of Biomechanical Engineering. Manuscript received February 20, 2013; final manuscript received August 16, 2013; accepted manuscript posted September 6, 2013; published online September 26, 2013. Assoc. Editor: Stephen M. Klisch.

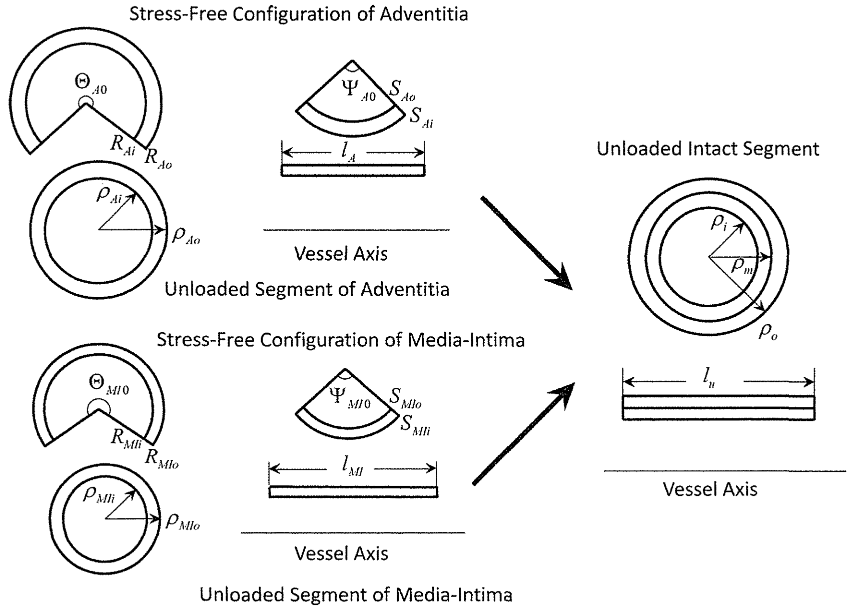

Fig. 1 Schematic drawing of the circumferential stress-free sectors and the axial stress-free arcs, the unloaded segments for adventitia and media-intima, and the unloaded intact segment

$$R_{\alpha\beta\mu\nu} = \frac{1}{2}\left(\frac{\partial^2\eta_{\alpha\nu}}{\partial\xi^\beta\partial\xi^\mu} + \frac{\partial^2\eta_{\beta\mu}}{\partial\xi^\alpha\partial\xi^\nu} - \frac{\partial^2\eta_{\alpha\mu}}{\partial\xi^\beta\partial\xi^\nu} - \frac{\partial^2\eta_{\beta\nu}}{\partial\xi^\alpha\partial\xi^\mu}\right) + \eta^{\delta\varepsilon}\left(\Gamma_{\delta\alpha\nu}\Gamma_{\varepsilon\beta\mu} - \Gamma_{\delta\alpha\mu}\Gamma_{\varepsilon\beta\nu}\right) \tag{3}$$

where $\eta^{\delta\varepsilon}$ denotes reciprocal components of the metric tensor $\eta_{\alpha\beta}$ and $\Gamma_{\delta\alpha\nu}$ the Christoffel symbols of the first kind with $\eta_{\alpha\beta}$. The Riemann–Christoffel tensor is used to determine whether the Riemannian stress-free configuration is Euclidean or not. In the three-dimensional space, distinct covariant components of the Riemann–Christoffel tensor $R_{1212} = R_{\vartheta\zeta\vartheta\zeta}$, $R_{1313} = R_{\vartheta\rho\vartheta\rho}$, $R_{2323} = R_{\zeta\rho\zeta\rho}$, $R_{1213} = R_{\vartheta\zeta\vartheta\rho}$, $R_{2123} = R_{\zeta\vartheta\zeta\rho}$, $R_{3132} = R_{\rho\vartheta\rho\zeta}$ may not vanish [15]. Therefore, we are allowed to only check the above six components of the Riemann–Cristoffel tensor.

Arterial sectors of rings cut radially and axial arcs sectioned from an adventitia and a media-intima of a vessel segment are schematically shown in Fig. 1. We assume that the infinitesimally thin sliced sectors and narrow curled axial strips are stress free. For the unloaded configurations, the principal stretch ratios of circumferential, axial, and radial directions with regard to the stress-free configurations are determined by the following equations:

$$\begin{aligned} \Lambda_{X\vartheta} &= \frac{2\pi\rho_X}{\Theta_{X0}R_X} = \sqrt{\frac{\gamma_{X\vartheta\vartheta}}{\eta_{X\vartheta\vartheta}}} \quad (R_{Xi} \le R_X \le R_{Xo}, \rho_{Xi} \le \rho_X \le \rho_{Xo}) \\ \Lambda_{X\zeta} &= \frac{l_X}{\Psi_{X0}S_X} = \sqrt{\frac{\gamma_{X\zeta\zeta}}{\eta_{X\zeta\zeta}}} \quad (S_{Xo} \le S_X \le S_{Xi}) \\ \Lambda_{X\rho} &= \frac{d\rho_X}{dR_X} = -\frac{d\rho_X}{dS_X} = \sqrt{\frac{\gamma_{X\rho\rho}}{\eta_{X\rho\rho}}} \end{aligned} \tag{4}$$

where X denotes A (adventitia) or MI (media-intima), and ρ_X, R_X, and S_X are radius of a material point p_X in each unloaded configuration, the stress-free circumferential sector, and the arc of the axial strip of adventitia or media-intima, respectively. The length of l_X denotes the axial length of the unloaded segment of adventitia or media-intima. Here, it should be noted that X is not a subscript that indicates a covariant tensor component. The angles are expressed in radians. The last line in Eq. (4) results in $S_{Xi} - S_X = R_X - R_{Xi}$. This equation implies that the thickness of a circumferential strip is equal to the axial one. This is consistent with the experiment [5]. Because the configuration ϑ_X, ζ_X, and ρ_X with $\eta_{X\alpha\beta}$ was assumed as a Riemannian stress-free configuration, the following relationships are derived from Eq. (4):

$$\eta_{X\vartheta\vartheta} = \left(\frac{\Theta_{X0}R_X}{2\pi}\right)^2, \quad \eta_{X\zeta\zeta} = \left(\frac{\Psi_{X0}S_X}{l_X}\right)^2, \quad \eta_{X\rho\rho} = \left(\frac{dR_X}{d\rho_X}\right)^2 = \left(\frac{dS_X}{d\rho_X}\right)^2 \tag{5}$$

and $\eta_{X\alpha\beta} = 0(\alpha \ne \beta)$. In this case, Eq. (3) shows that a covariant component of the Riemann–Christoffel tensor for adventitia or media-intima is as follows:

$$R_{X\vartheta\zeta\vartheta\zeta} = \left(\frac{\Theta_{X0}\Psi_{X0}}{2\pi l_X}\right)^2 R_X S_X \tag{6}$$

The other five components vanish. The nonvanishing Riemann–Christoffel tensor implies that the Riemannian stress-free configuration is not Euclidean.

Because the incompressibility of the arterial wall [16] results in $\Lambda_{X\vartheta}\Lambda_{X\zeta}\Lambda_{X\rho} = 1$, the relationship between ρ_X and R_X is given by the following equation:

$$\rho_X = \sqrt{\frac{\Theta_{X0}\Psi_{X0}}{6\pi l_X}\left\{-2R_X^3 + 3(R_{Xi} + S_{Xi})R_X^2 - (R_{Xi} + 3S_{Xi})R_{Xi}^2\right\} + \rho_{Xi}^2} \tag{7}$$

It is easily demonstrated that $\rho_{Xi} = \rho_X(R_{Xi})$ and ρ_X increases as R_X increases for $R_X \in [R_{Xi}, R_{Xo}]$. For the unloaded intact state, the deformation may be described with regard to the unloaded configuration of the media-intima

$$\vartheta = \vartheta_{MI}, \quad \zeta = \tilde{\Lambda}_{MI\zeta}\zeta_{MI}, \quad \rho = \sqrt{\frac{\rho_{MI}^2 - \rho_{MIi}^2}{\tilde{\Lambda}_{MI\zeta}} + \rho_i^2} \tag{8}$$

where $\tilde{\Lambda}_{MI\zeta} = l_u/l_{MI}$. The deformation of the unloaded intact state with regard to the unloaded state of the adventitia may be described as follows:

$$\vartheta = \vartheta_A, \quad \zeta = \tilde{\Lambda}_{A\zeta}\zeta_A, \quad \rho = \sqrt{\frac{\rho_A^2 - \rho_{Ai}^2}{\tilde{\Lambda}_{A\zeta}} + \rho_m^2} \tag{9}$$

where $\tilde{\Lambda}_{A\zeta} = l_u/l_A$ and the radius ρ_m is given by the Eq. (8)

$$\rho_m = \sqrt{\frac{\rho_{MIo}^2 - \rho_{MIi}^2}{\tilde{\Lambda}_{MI\zeta}} + \rho_i^2} \tag{10}$$

The other stretch ratios of the unloaded intact configuration with regard to each unloaded separate configuration are defined as follows:

$$\tilde{\Lambda}_{X\vartheta} = \frac{\rho}{\rho_X}, \quad \tilde{\Lambda}_{X\rho} = \frac{d\rho}{d\rho_X} \tag{11}$$

For the axially stretched and pressurized state, the deformation may be described with regard to the unloaded intact state

$$\theta = \vartheta, \quad z = \tilde{\lambda}_z\zeta, \quad r = \sqrt{\frac{\rho^2 - \rho_i^2}{\tilde{\lambda}_z} + r_i^2} \tag{12}$$

where $\tilde{\lambda}_z$ denotes a constant axial stretch ratio with regard to the unloaded intact state. The stretch ratios of the loaded state with regard to the stress-free states are as follows:

$$\lambda_\theta = \frac{r}{\rho}\tilde{\Lambda}_{X\vartheta}\Lambda_{X\vartheta}, \quad \lambda_z = \tilde{\lambda}_z\tilde{\Lambda}_{X\zeta}\Lambda_{X\zeta}, \quad \lambda_r = \frac{dr}{d\rho}\tilde{\Lambda}_{X\rho}\Lambda_{X\rho} \tag{13}$$

where we need values of R_{Xi}, R_{Xo}, S_{Xi}, Θ_{X0}, Ψ_{X0}, R_X, l_u, $\tilde{\lambda}_z$, and r_i to compute λ_k $(k = \theta, z, r)$ at a radius $r(R_X)$ in a deformed configuration. Because an artery is cylindrically orthotropic [17], intraluminal pressurization and constant axial stretch result in no shear strains in the cylindrical coordinate system.

2.2 Strain Energy Function. In this study, the Fung-type strain energy density function [9] was used to analyze the stress distributions for the porcine common carotid artery. For the human common carotid artery, a structurally-based strain energy function [13,14] was used. This function is described as follows:

$$W = \frac{\mu}{2}(I_1 - 3) + \frac{k_1}{k_2}(\exp Q - 1)$$

$$Q = k_2\left\{(1-\varsigma)(I_1 - 3)^2 + \varsigma(I_4 - 1)^2\right\} \tag{14}$$

$$I_1 = \lambda_\theta^2 + \lambda_z^2 + \lambda_r^2, \quad I_4 = \lambda_\theta^2\cos^2\varphi + \lambda_z^2\sin^2\varphi$$

where μ and k_1 denote constants with the dimension of energy density, k_2 and $\varsigma \in [0, 1]$ dimensionless constants. The angle φ may be interpreted as the (mean) angle between the fiber direction and the circumferential direction. These constants are different between the media-intima and the adventitia. The invariant I_4 is larger than 1. If I_4 becomes smaller than 1 in computing, it must be set 1. For the incompressibility of the arterial wall [16], the Lagrange multiplier H is introduced in the stress-strain relationship. Therefore, the components of the Cauchy stress are as follows:

$$\sigma_{kk} = -H + \lambda_k\frac{\partial W}{\partial \lambda_k}(k = \theta, z, r) \tag{15}$$

where the summation convention with subscripts is not used.

2.3 Equilibrium Condition for the Cauchy Stress. The only nontrivial equilibrium equation for the physical components of the Cauchy stress is as follows:

$$\frac{d\sigma_{rr}}{dr} + \frac{\sigma_{rr} - \sigma_{\theta\theta}}{r} = 0 \tag{16}$$

The boundary conditions are as follows:

$$\sigma_{rr}(r_i) = -P_i, \quad \sigma_{rr}(r_o) = -P_o = 0 \tag{17}$$

where r_i and r_o denote the inner and outer radii of the vessel, respectively, and P_i is the intraluminal pressure. The radial stress is integrated as follows:

$$\sigma_{rr}(a) = \int_a^{r_o}\frac{\sigma_{rr}(r) - \sigma_{\theta\theta}(r)}{r}dr \quad (r_i \le a \le r_o) \tag{18}$$

The circumferential stress $\sigma_{\theta\theta}$ and the axial stress σ_{zz} have discontinuity at the boundary r_m between the media-intima and the adventitia, while the radial stress σ_{rr} is continuous. From the boundary condition at the inner surface, the intraluminal pressure results in the following:

$$P_i = \int_{r_i}^{r_o}\frac{\sigma_{\theta\theta} - \sigma_{rr}}{r}dr \tag{19}$$

An axial force F_z is calculated by the following equation:

$$F_z = -\pi r_i^2 P_i + 2\pi\int_{r_i}^{r_o}\sigma_{zz}r dr = 2\pi\int_{r_i}^{r_o}\left\{\sigma_{zz} - \frac{1}{2}(\sigma_{\theta\theta} + \sigma_{rr})\right\}r dr \tag{20}$$

The above two integrals may be numerically determined with an inner radius and axial stretch ratio with regard to the unloaded configuration if the stress-free configurations and the strain energy functions are provided. Since for the provided configuration of the unloaded state the intraluminal pressure and the axial force do not vanish in the calculation, we take the numerically obtained values ρ_i', ρ_m', ρ_o', and l_u' to satisfy $P_i = 0$ and $F_z = 0$ as an adjusted unloaded intact configuration. Thereafter, we compute the residual stress and strain.

3 Results

The distributions of stretch ratios and stresses through the wall thickness in the one-layer model of the porcine common carotid artery in the unloaded state and those under a physiological condition ($P_i = 16$ kPa, $\tilde{\lambda}_z = 1.5$) were computed using the dataset from the study of Wang and Gleason [9]. Figure 2 shows the stretch ratios and stresses under the unloaded condition considering the curl of the axial strip sectioned from the artery. Figure 3 shows the stretch ratios and stresses under the physiological condition. The circumferential stress was almost uniform through the wall thickness, whereas the axial stress was a higher gradient compared with that only accounting for an opening angle of the circumferential sector, which is defined as the angle subtended between two lines originating from the midpoint to the tips of the inner surface of a radial section of the vessel ring. Wang and Gleason [9] adopted the same assumption on the residual strains, although they performed an approximate analysis based on one-layer model. If the present method was used, different constants in the strain energy function might have been obtained from the same experiment [9]. However, the distributions of stress under the physiological condition show almost the same pattern as the results by Wang and Gleason [9], whereas the magnitude of the circumferential and axial stresses is rather larger than that reported previously [9].

We computed the stretch ratios and stresses based on the two-layer model described in the method section of the present paper from the dataset of Sommer et al. [12] and Sommer and Holzapfel [14]. Because we lacked some of data to compute the distributions of stresses, we had to assume plausible values. The dataset used in the computing are shown in Tables 1 and 2. The axial stretch

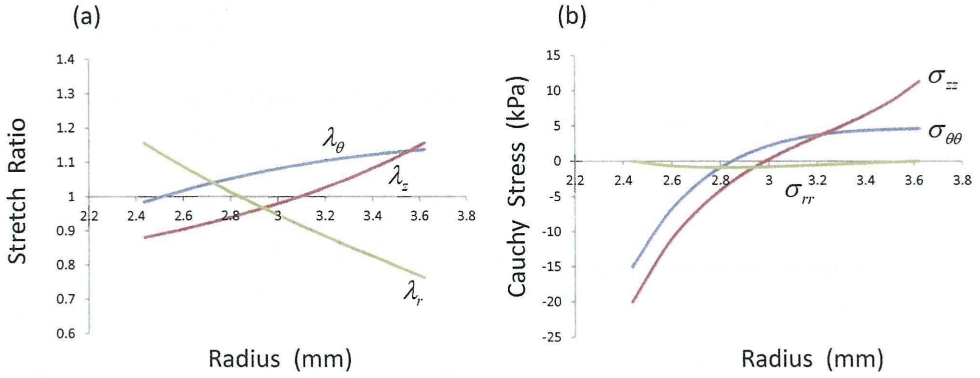

Fig. 2 Residual stretch ratios (*a*) and residual stresses (*b*) based on one-layer model accounting for circumferential opening sector and axial arc dissected from a porcine common carotid artery. Radius denotes that of the unloaded configuration.

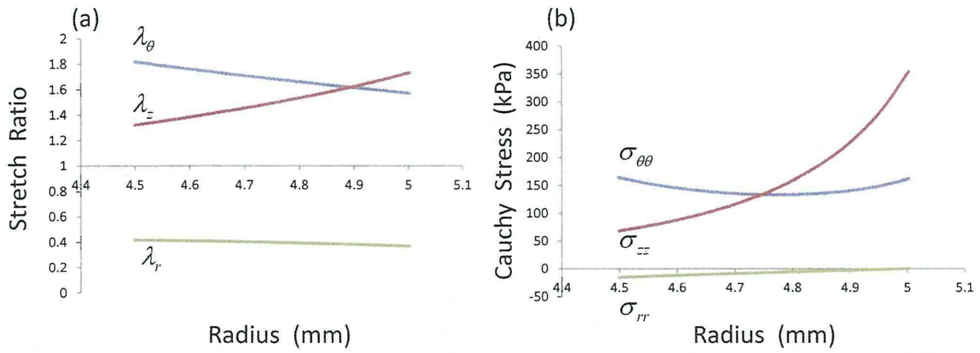

Fig. 3 Stretch ratio (*a*) and stress (*b*) distributions under a physiological load accounting for circumferential opening sector and axial arc dissected from a porcine common carotid artery. Radius denotes that of the physiologically loaded configuration.

Table 1 Dimensions for stress-free configurations of media-intima (*MI*) and adventitia (*A*) estimated from the data in reference [12]. Axial length l_u of the unloaded intact segment was 15 mm.

Media-Intima
$R_{MIi}=5.917$ mm, $R_{MIo}=6.617$ mm, $\Theta_{MI0}=187.3$ deg
$S_{MIi}=71.429$ mm, $S_{MIo}=70.729$ mm, $\Psi_{MI0}=12.34$ deg

Adventitia
$R_{Ai}=4.184$ mm, $R_{Ao}=4.654$ mm, $\Theta_{A0}=306.7$ deg
$S_{Ai}=8.000$ mm, $S_{Ao}=7.530$ mm, $\Psi_{A0}=102.5$ deg

Table 2 Constants in strain energy function determined accounting for circumferential and axial residual strains for media-intima and adventitia of human common carotid artery in reference [14]. The method of analysis [14] is different from that described in the present paper.

	μ (kPa)	k_1 (kPa)	k_2	φ (deg)	ς
Media-Intima	122.3	24.7	16.5	6.9	0.8
Adventitia	59.6	180.9	109.8	30.1	0.8

ratios $\tilde{\Lambda}_{MI\zeta}=0.98$ and $\tilde{\Lambda}_{A\zeta}=1.08$ (mean values of segments) were observed in the study of Sommer et al. [12].

Figure 4 shows the residual stretch ratios and stresses. Discontinuity at the radius of the boundary between the media-intima and the adventitia is evident. The circumferential stretch ratio was compressive on the inner side and tensile on the outer side in the media-intima and the same pattern appeared in the adventitia, whereas the circumferential stretch ratio was almost 1 through the adventitia region. The axial stretch ratio was compressive in the media-intima, whereas it was tensile in the adventitia. The residual stresses of the circumferential and axial directions increased from the inner surface to the outer surface although there was the discontinuity at the boundary between the media-intima and the adventitia.

Under a physiological condition ($P_i=16$ kPa, $\tilde{\lambda}_z=1.1$), the stretch ratios and stresses were computed and they are shown in Fig. 5. The circumferential and axial stresses increased from the inner surface to the outer surface in the loaded intact arterial wall, although there was the discontinuity at the boundary between the media-intima and the adventitia. This result was different from that expected from the porcine common carotid artery. These high gradient distributions of stress may not match homeostatic function of living organs although we could not avoid these results.

4 Discussion

In this study, we have proposed a method to analyze the stress distributions of a thick-walled artery considering both circumferential and axial residual strains. Holzapfel et al. [5] have measured the curvatures of strips sectioned from adventitia, media, and intima for the human abdominal aorta. Their results showed that strips of the adventitia appear to be relatively flat in the both directions, while strips of the media exhibit negative curvatures in both directions. Circumferential strips of the intima have pronounced positive curvatures, while axial strips are relatively flat. These data show that Eqs. (4)–(7) in the present study are not valid in some cases. If the opening angles of strips are π(rad), i.e., the strips are flat, at least in one direction, the mathematical model

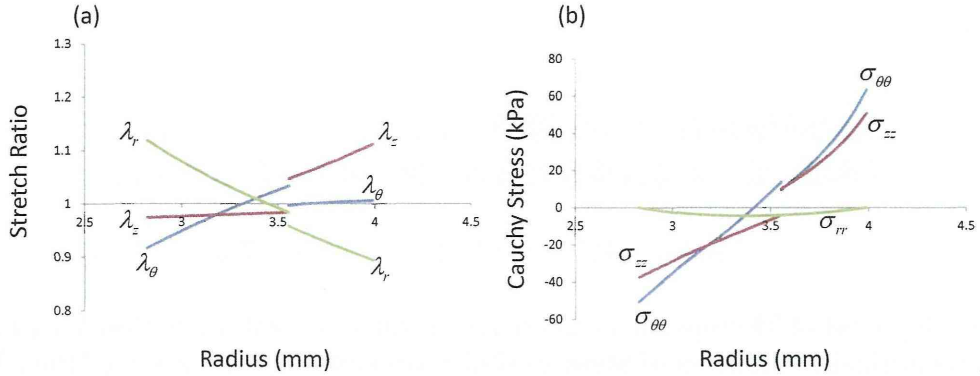

Fig. 4 Residual stretch ratios (*a*) and residual stresses (*b*) based on two-layer model accounting for circumferential sectors and axial arcs of media-intima and adventitia dissected from a human common carotid artery. Radius denotes that of the unloaded intact configuration.

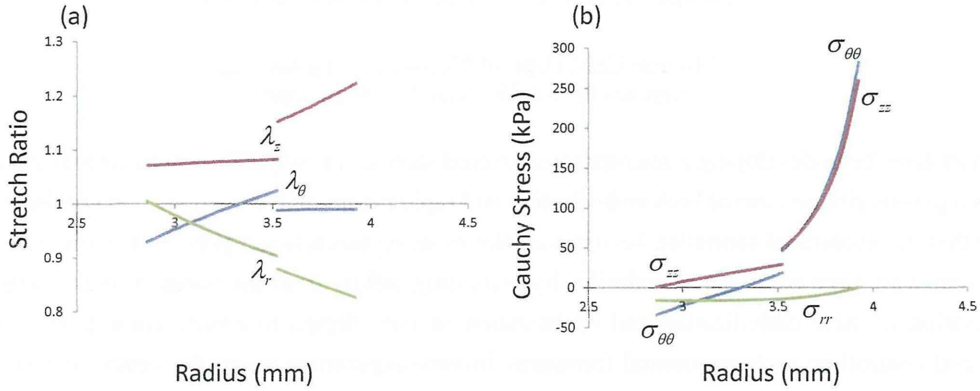

Fig. 5 Stretch ratio (*a*) and stress (*b*) distributions under a physiological load accounting for circumferential opening sectors and axial arcs of media-intima and adventitia dissected from a human common carotid artery. Radius denotes that of the physiologically loaded configuration.

proposed by Holzapfel and Ogden [6] should be applied to analyze the stress distributions in a vessel wall.

Sommer et al. [12] and Sommer and Holzapfel [14] studied human carotid arteries with intact wall and dissected layers. We analyzed stress distributions in the two-layer model for their human common carotid artery. We found that the distributions of the circumferential and axial stresses increase from the inner surface to the outer surface under physiological conditions considering both circumferential and axial residual strains estimated from previously published data [12] and using mean values of constants [14] in the strain energy function proposed by Holzapfel et al. [13]. However, our analysis may not be reliable because of the uncertainty of center angles of Θ_{X0} and Ψ_{X0} for each layer. Even so, in the aged human carotid arteries [14], the residual strains might result in a high gradient of the stress distribution instead of a uniform distribution. If the present result is correct, the residual stress in arteries may not necessarily induce uniform stress distributions under physiological loadings.

References

[1] Fung, Y. C., 1984, *Biodynamics: Circulation*, Springer-Verlag, New York.

[2] Chuong, C. J., and Fung, Y. C., 1986, "On Residual Stress in Arteries," ASME J. Biomech. Eng., **108**(2), pp. 189–192.

[3] Vossoughi, J., 1992, "Longitudinal Residual Strains in Arteries," Proceedings of the 11th Southern Biomedical Engineering Conference, Memphis, TN, pp. 17–19.

[4] Vossoughi, J., Hedjazi, Z., and Borris, F. S., 1993, "Intimal Residual Stress and Strain in Large Arteries," *Proceedings of the Summer Bioengineering Conference*, N. A. Langrana, M. H. Friedmann, and E. S. Groods, eds., Am Soc Mech Eng Bioeng Div., New York, Vol. 24, pp. 434–437.

[5] Holzapfel, G. A., Sommer, G., Auger, M., Regitnig, P., and Ogden, R. W., 2007, "Layer-Specific 3D Deformations of Human Aortas With Non-Atherosclerotic Intimal Thickening," Ann. Biomed. Eng., **35**, pp. 530–545.

[6] Holzapfel, G. A., and Ogden, R. W., 2010, "Modelling the Layer-Specific Three-Dimensional Residual Stresses in Arteries, With an Application to the Human Aorta," J. R. Soc. Interface, **7**, pp. 787–799.

[7] Fung, Y. C., Fronek, K., and Patiucci, P., 1979, "Pseudoelasticity of Arteries and the Choice of its Mathematical Expression," Am. J. Physiol. Heart Circ. Physiol., **237**, pp. H620–H631.

[8] Chuong, C. J., and Fung, Y. C., 1983, "Three-Dimensional Stress Distribution in Arteries," ASME J. Biomech. Eng., **105**(3), pp. 268–274.

[9] Wang, R., and Gleason, R. L., 2010, "A Mechanical Analysis of Conduit Arteries Accounting for Longitudinal Residual Strains," Ann. Biomed. Eng., **38**, pp. 1377–1387.

[10] Takamizawa, K., and Matsuda, T., 1990, "Kinematics for Bodies Undergoing Residual Stress and its Applications to the Left Ventricle," ASME J. Appl. Mech., **57**(2), pp. 321–329.

[11] Takamizawa, K., 1991, "Stress-Free Configuration of a Thick-Walled Cylindrical Model of the Artery: An Application of Riemann Geometry to the Biomechanics of Soft Tissues," ASME J. Appl. Mech., **58**(3), pp. 840–842.

[12] Sommer, G., Regitnig, P., Költringer, L., and Holzapfel, G. A., 2010, "Biaxial Mechanical Properties of Intact and Layer-Dissected Human Carotid Arteries at Physiological and Supraphysiological Loadings," Am. J. Physiol. Heart Circ. Physiol., **298**, pp. H898–H912.

[13] Holzapfel, G. A., Sommer, G., Gasser, C. T., and Regitnig, P., 2005, "Determination of Layer-Specific Mechanical Properties of Human Coronary Arteries with Nonatherosclerotic Intimal Thickening and Related Constitutive Modeling," Am. J. Physiol. Heart Circ. Physiol., **289**, pp. H2048–H2058.

[14] Sommer, G., and Holzapfel, G. A., 2012, "3D Constitutive Modeling of the Biaxial Mechanical Response of Intact and Layer-Dissected Human Carotid Arteries," J. Mech. Behav. Biomed. Mater., **5**, pp. 116–128.

[15] Sokolnikoff, I. S., 1964, *Tensor Analysis*, John Wiley & Sons, Inc., New York.

[16] Carew, T. E., Vaishnav, R. N., and Patel, D. J., 1968, "Compressibility of the Arterial Wall," Circ. Res., **23**, pp. 61–68.

[17] Patel, D. J., and Fry, D. L., 1969, "The Elastic Symmetry of Arterial Segments in Dogs," Circ. Res., **24**, pp. 1–8.

日本機械学会論文集（B 編）
79 巻 801 号（2013-5）

原著論文 No. 2013-JBR-0093

脳動脈瘤治療用多孔薄膜カバードステントの開発*
（薄膜留置による瘤塞栓性能の評価と微細孔形状の最適化）

田地川 勉[*1]，中川 雄太[*2]，紅林 芳嘉[*2]，西 正吾[*3]，中山 泰秀[*4]

Development of Microporous Covered Stent for Cerebral Aneurysm Treatment
(Hydrodynamical Evaluation of Stent Embolization and Optimization of Pore Design of Microporous Film)

Tsutomu TAJIKAWA[*1], Yuta NAKAGAWA, Yoshio KUREBAYASHI,
Shogo NISHI and Yasuhide NAKAYAMA

[*1] Kansai Univ. Dept. of Mechanical Engineering
Yamate-cho 3-3-35, Suita, 564-8680 Japan

The authors have been developing a microporous covered stent as a newly device for cerebral aneurysm treatment. This stent has a porous film to control both embolization and rapid neointimal formation. According to previous study, it is expected that the neointimal formation becomes earlier by using much larger pores. But there is a possibility that the covered stent with large pare cannot embolize by increasing inflow from the parent vessel. The purpose of this study is estimation of stent embolization and optimization of pore design to ensure compatibility between reliable embolization and controlling early neointimal formation, in-vitro experiment under the steady flow condition based on flow similarity law has been conducted by using a two dimensional parent vessel model with a saccular aneurysm model and simplified micro-porous film models. The PIV results show that mean shear rate in the aneurysm model after stenting, of which pore diameter is <300μm and porosity is 60%, was decreased to less than 1/10 of before stenting. According to flow visualization, it is considered that viscous shear force caused by shear flow in the vicinity of the parent vessel wall drives the blood in the aneurysm cavity passing through the micro-pores on the film. As the result of the driving force estimating, it is suggested that ratio of the viscous shear force to rotational moment of the blood in the aneurysm cavity is one of the important hydrodynamical parameter to estimate the flow pattern in aneurysm and the stent embolization.

Key Words : Micro-Porous Covered Stents, Micropores Film, Aneurysm, Embolization, Shear Rate, In-Vitro Experiment

1. 緒　言

脳動脈瘤は，脳組織や神経に囲まれた血管に発生し，血管も動脈瘤も小さいことから，その治療が難しい血管疾患であり，破裂に至ると致死率が非常に高いため，その早期発見と早期治療が求められている．現在，治療法としては，動脈瘤のネック部を金属クリップで止める外科的治療や，カテーテルで動脈瘤内にコイル状のワイヤーを誘導し，ワイヤーを瘤内に留置することで，瘤内の血栓形成を促進して瘤内腔を塞ぐ血管内治療が行われている．しかし瘤が大きい場合や瘤の開口（ネック）部が広い場合，あるいは瘤が脳深部にある場合には，クリッピングできなかったり，コイルが留置できなかったりする場合があり，またコイルが留置できても十分に塞栓で

---

* 原稿受付　2013 年 1 月 31 日

[*1] 正員，関西大学　システム理工学部（〒564-8680　大阪府吹田市山手町 3-3-35）
[*2] 学生員，関西大学大学院　理工学研究科　システムデザイン専攻
[*3] 札幌東徳洲会病院　脳神経外科
[*4] 国立循環器病研究センター　生体医工学部　医工学材料研究室
E-mail: tajikawa@kansai-u.ac.jp

きない場合や後遺症を煩うリスクがあるなど，瘤破裂リスクと治療リスクを比較し，明らかに破裂のリスクが高まってから治療が行われているのが現状である．このため未破裂動脈瘤を，経過観察などすること無く，より低侵襲・簡便・確実に治療できるデバイスの開発が望まれている．

そこで本研究では，これら治療法に取って代わる新しい治療用デバイスとして図1に示すようなカバードステントの開発を行っている(1-5)．先に述べた治療法と比べ，ステント留置法はカテーテル治療のためコイル塞栓術と同様に低侵襲で治療できる利点がある．本カバードステントの構造的特徴は，Ni-Ti 製ステントストラットをポリウレタン製薄膜で覆い，瘤を塞栓する過程でステント内腔に血管壁内膜組織が形成されやすいよう，カバー薄膜を直径数百ミクロンの円型孔によって多孔化されていることである．一般的なカバードステントを血管内に留置するとステント内腔面が内膜組織の形成によって肥厚しながら最終的に内腔が内膜化されていくが，小血管の場合内膜組織の形成の制御が難しく，肥厚しやすいため，内膜化完了前に閉塞に至る場合がある．そこで本ステントでは,カバー薄膜を多孔化することで血管内皮細胞が微細孔を通過して内腔面に移動できるようになるため,早期に内皮化を完了させることができ，過剰な肥厚を抑制できるという特徴を有している(3)．

過去に行った動物実験で，微細孔の開口率を12.6%から23.6%に増加させることで，確実な動脈瘤塞栓能を維持しながら，内膜組織の形成による内膜肥厚を抑制し，内腔面を内皮化できた(4-5)．さらに薄膜の開口率を増やすことで,より早期に内皮化できることが期待されるが,開口の増加によって動脈瘤内の血流が十分に抑制できず,塞栓性能が低下することが懸念される．

そこで本研究では，カバー薄膜に加工する微細孔の直径と開口率の最適化を目的として、円型孔の直径と開口率を系統的に変化させた微細多孔膜を作製し、それを2次元動脈瘤モデルのネック部に設置し，生理的流れ条件下で瘤内流れの可視化を行うことで，その留置効果を定性的に調べた．また瘤内の流速分布をPIVによって計測し，流体力学に基づいてカバー薄膜の塞栓能を定量評価する試みを行い，得られた結果を使って，大きな開口を有しながら塞栓能も両立した微細孔の最適設計を提案したので報告する．

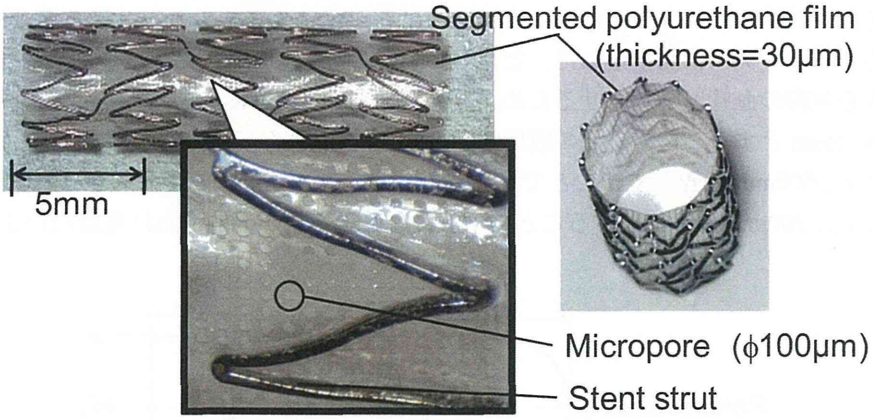

Fig. 1　Prototype of Micro-porous covered stent.

2. 実験装置および方法

本研究では，カバー薄膜の血流抑制効果による瘤塞栓能の定量評価と微細孔の設計最適化を目的としていることから，個体差の影響の大きい動物実験では無く，所望の条件を再現することで繰り返し実験可能で，かつ定量評価可能な生体外模擬実験を行った．生体外模擬実験を行う場合，生体内の全ての現象を生体外で再現しようとすると，モデルの作製や計測・評価が難しくなったり，結果に一般性が無くなったりする恐れがある．そこで本研究では，動脈瘤内の血流動態を再現するために，流体力学理論と力学的相似則に基づいて，動脈瘤モデルの設計と実験条件の設定を行った．以下に，その詳細について説明する．

2・1　脳動脈瘤および親血管血流モデル

本研究では，本カバードステントが治療対象としている直径 D=3～6mm の脳動脈を留置対象の親血管と想定し実験条件の設定を行った．文献[6-8]を参考に，これらの血管を流れる平均血流量を Q=0.1～0.6L/min，心拍数を 60～100bpm（f=1,00～1.67Hz），血液の密度と粘度をρ=1040kg/m^3，μ=4.62mPa･s（動粘度ν=4.44mm^2/s）と設定した．対象となる親血管内流れの Reynolds 数（Re）と Womersley 数（α）は，それぞれ

$$Re \equiv \frac{\overline{U}D}{\nu} = \frac{4Q}{\pi D\nu} \tag{1}$$

$$\alpha \equiv \frac{D}{2}\sqrt{\frac{2\pi f}{\nu}} \tag{2}$$

と定義した．ここで D は親血管直径，$\overline{U}$は親血管断面平均流速，νは血液の動粘性係数，f は拍動周波数である．上記設定条件を基に，これら無次元パラメータを計算するとそれぞれ，Re=170～960，α=1.78～4.61 であった．これらのことから，親血管内の流れは層流であり，α<5 であれば準定常流れと見なすことができる[9]ことから，流れの力学的相似則に基づき親血管内の流れが同じ Reynolds 数の定常流れでほぼ相似できると考え，定常流れ条件下で親血管の Reynolds 数をパラメータとして実験することとした．

図2に実験で使用した脳動脈モデルを示す．血管モデルとしては，親血管の直径が D=5mm，瘤が親血管側壁に形成される嚢状型（side-wall）とした．動脈瘤モデルは，瘤直径を親血管直径の2倍の D_a=10mm の球形ドーム型，瘤高さを H_a=9.1mm，瘤ネック部直径（ネック幅）を N=7.06mm，親血管壁から動脈瘤最大直径までの高さを S=4.1mm，ネック部のフィレット半径 C を C=0.4mm とし，瘤深さとネック幅の比で表されるアスペクト比が AR=1.29 と，治療の判断基準であるアスペクト比 AR=1.5~1.6[10-12]をやや下回り，これまであまり積極的に治療されていない大きさに設定した．なお実際の動脈瘤と親血管は3次元的な形状を有しているが，これではモデル内流れが2次流れを伴う複雑な流れとなるため，本研究では親血管は直管とし，親血管と瘤はそれらを側面から投影した形を有する2次元モデルに簡単化した．ただし，2次元動脈瘤モデルおよび親血管モデル内で流れによって生じる圧力損失を実際の血管と一致させるため，親血管モデルの流路幅を H_{PV}=5mm，親血管と動脈瘤の奥行きを流路幅と同じ W=5mm とすることで，元の親血管と水力平均直径が一致するようにした．また，瘤モデル上流側の親血管長さは L_{in}=500mm 直管とすることで流れを十分に発達させた状態で流入させると共に，瘤モデル下流側の親血管長さを L_{out}=200mm の直管とすることで下流側配管の影響が瘤内流れに及ばないようにした．

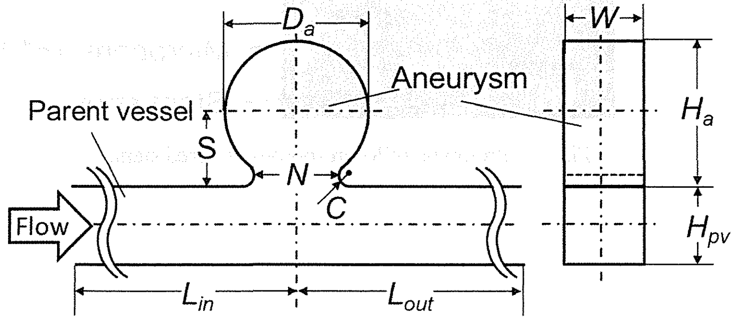

Fig. 2　Schematic diagram of simplified 2-dimansional cerebral aneurysm model.

2・2　カバードステントモデル

本研究で開発しているカバードステントは，Ni-Ti 製のステントストラットをセグメント化ポリウレタンにディッピングすることで厚さ 20～30μm の薄膜を形成した後，KrF エキシマレーザーを使ったレーザー加工機によって薄膜を多数の微細円孔で搾孔することで多孔化している[4, 5, 13-15]．ここでベアステントのストラット間の空隙ピッチは，微細孔直径と比べて十分に広いため，本カバードステントを使った治療では流れの抑制効果のほとんどがカバー薄膜によると考えられることから，実験モデルではステントストラットを省略し，多孔薄膜モデルだけを2次元動脈瘤モデルネック部に設置することとした．